

Phase stability and precipitation in L1₂-strengthened CoCrNi medium-entropy alloys at intermediate temperatures

J.Y.C. Fang^a, W.H. Liu^b, J.H. Luan^c, Z.B. Jiao^{a,*}

^a *Department of Mechanical Engineering, The Hong Kong Polytechnic University, Hong Kong, China*

^b *School of Materials Science and Engineering, Harbin Institute of Technology (Shenzhen), Shenzhen, China*^c

Department of Materials Science and Engineering, City University of Hong Kong, Hong Kong, China

**Corresponding author: zb.jiao@polyu.edu.hk*

Abstract

Understanding phase stability and precipitation at intermediate temperatures is crucial for tailoring microstructures and mechanical properties of L1₂-strengthened multicomponent alloys. In this study, the precipitate type, morphology, and distribution of (CoCrNi)_{100-2x}(AlTi)_x (x=3, 5, and 7 at. %) medium-entropy alloys (MEAs) at 600-900 °C were systematically investigated through a combination of scanning electron microscopy, energy dispersive X-ray spectroscopy, X-ray diffraction, electron backscatter diffraction, and thermodynamic calculations. Our results reveal that the Al and Ti additions promote the destabilization of supersaturated fcc into L1₂ and σ phases, and the dominating phases of the MEAs change from fcc + L1₂ to fcc + L1₂ + σ and to L1₂ + σ + L2₁ phases as the Al and Ti concentrations increase. In addition, increasing the temperature leads to a change of precipitate morphology from lamellar to granular microstructures. The effects of alloying additions and aging temperature on the phase stability, precipitation behavior, and mechanical properties of the MEAs were discussed from the thermodynamic and kinetic points of view.

Keywords: medium entropy alloy; precipitation; phase relation; precipitate microstructure

1. Introduction

Medium/high-entropy alloys (M/HEAs) have been emerging as a new class of metallic materials due to their unique microstructure and superior mechanical properties ^[1-5]. The medium/high-entropy alloy-design strategy shifts our exploration of new metallic materials from the corners of phase diagrams to less explored centers. In contrast to the conventional wisdom that compositionally complex alloys tend to form complicated phases or intermetallic compounds, M/HEAs with multi-principal elements crystallize into simple solid-solution phases. Particularly, face-centered cubic (fcc) M/HEAs exhibit exceptional mechanical properties at cryogenic temperatures, making them attractive for structural applications ^[5-7]. However, these solid-solution alloys exhibit low strength at ambient and elevated temperatures, which severely restricts their practical uses. Precipitation hardening has been proved to be an effective method to increase the mechanical strength of M/HEAs ^[8]. Particularly, the uniform precipitation of coherent L1₂ nanoparticles can effectively strengthen M/HEAs without causing a significant reduction in ductility, opening a new space for the development of advanced structural materials with excellent mechanical properties at both room and elevated temperatures ^[9-21]. Understanding the phase stability and precipitation is crucial for tailoring the precipitate microstructure and mechanical properties of coherent precipitation-strengthened M/HEAs, and considerable effort has been devoted to determining the phase relations in L1₂-strengthened M/HEAs. For instance, He et al. ^[19] found that fine-scale coherent L1₂ precipitates can be formed in CoCrFeNi alloys with proper amounts of Al and Ti, while excessive additions of Al and Ti induced the formation of brittle L2₁-(Ni,Co)₂TiAl Heusler precipitates, which degrade the mechanical properties by weakening grain boundaries. Gwalani et al. ^[22] reported that the L1₂ phase is metastable in a Al_{0.3}CoCrFeNi alloy at intermediate temperatures, which destabilizes into a stable B2-NiAl phase at 700 °C. Borkar et

al. ^[23] found that the predominant phases of the $Al_xCrCuFeNi_2$ alloys evolve from the duplex fcc + $L1_2$ to mixed fcc + $L1_2/BCC$ + B2 and eventually to BCC + B2 structures with increased Al concentrations. In addition, topologically closed-packed phases, such as σ phase, are also frequently observed in $L1_2$ -strengthened M/HEAs. For example, Lin et al. ^[24] reported that the fcc phase decomposes into fcc and σ phases in a $Al_5Cr_{32}Fe_{35}Ni_{22}Ti_6$ alloy at 700 and 800 °C, the formation of which leads to a significant decrease in fracture toughness. Thus, the previous investigations indicate that $L1_2$ -strengthened M/HEAs are not as stable as single-phase fcc M/HEAs at intermediate temperatures, and their phase relations and stability are quite sensitive to alloying additions and aging temperatures.

Recent studies reveal that $L1_2$ -strengthened CoCrNi MEAs have a great potential to get a good balance of mechanical properties across a wide range of temperatures. Zhao et al. ^[13] reported that the Al and Ti additions to the CoCrNi alloy induce the precipitation of nanoscale $L1_2$ precipitates, which leads to the development of $L1_2$ -strengthened MEAs with a tensile strength of ~1.3 GPa and a ductility of ~45%. Du et al. ^[25] further improved the mechanical properties of this alloy through tailoring a dual heterogeneous structure of both matrix and precipitates, achieving an ultrahigh tensile strength of 2.2 GPa and a uniform elongation of 13% at ambient temperature. Zhao et al. ^[26] found that the $L1_2$ -strengthened $(CoCrNi)_{94}Al_3Ti_3$ alloy exhibits remarkable thermal stability against coarsening at 800 °C, which is benefit from the sluggish diffusion of MEAs. An et al. ^[27] reported that the $L1_2$ -strengthened $(CoCrNi)_{95}Al_2Ti_2Ta_1$ MEA exhibits a yield strength of 620 MPa and a tensile strength of 939 MPa at 700 °C, which are higher than those of IN718 superalloys. The superior mechanical properties of $L1_2$ -strengthened CoCrNi-based MEAs make them promising candidates as structural materials for elevated-temperature applications. To date, however, the precipitate microstructure and its evolution in $L1_2$ -strengthened CoCrNi alloys have

not been systematically characterized. The effects of alloying additions and aging temperature on the phase relations of L1₂-strengthened CoCrNi alloys are yet to be assessed, and the fundamental understanding of phase stability and precipitation behavior of these alloys at intermediate temperatures has not yet been fully evolved.

In this study, we aim to understand the effects of alloying additions and aging temperature on the phase relations, precipitate microstructure, and mechanical properties of L1₂-strengthened CoCrNi MEAs at intermediate temperatures. Specifically, the crystal structure, morphology, chemical composition of various types of precipitates in the (CoCrNi)_{100-2x}(AlTi)_x (x=3, 5, and 7 at.%) alloys at 600-900 °C were systematically investigated through a combination of scanning electron microscopy (SEM), energy dispersive X-ray spectroscopy (EDS), X-ray diffraction (XRD), electron backscatter diffraction (EBSD), and thermodynamic calculations. Particular attention was paid to the key factors governing the phase stability and transformations of the L1₂-strengthened CoCrNi alloys at intermediate temperatures.

2. Experimental

The three alloys with nominal compositions of (CoCrNi)_{100-2x}(AlTi)_x (x=3, 5, and 7 at.%) were prepared by arc-melting a mixture of the constituent elements with purities better than 99.9 wt.% under a Ti-gettered argon atmosphere. Chemical compositions (at.%) of the three alloys are given in Table 1. For simplicity, these MEAs are hereafter referred to as Al₃Ti₃, Al₅Ti₅, and Al₇Ti₇ alloys. Ingots were melted five times to ensure chemical homogeneity and then drop-cast into a copper mold with a cavity of 50 × 15 × 3 mm³. The as-cast plates were homogenized for 3 h at 1150 °C and then cold-rolled for multiple passes, yielding a total reduction of approximately 70%. The rolled plates were subjected to recrystallization for 3 min at 1150 °C, followed by water quenching and then aging for 300 h at 600, 700, 800, and 900 °C. Heat-treated samples were

polished using standard mechanical polishing procedures and then electrochemically etched with a solution of HNO₃ (25%) and C₂H₅OH (75%) for 2 min at 20 V and -40 °C. The resulting microstructures were examined by SEM equipped with EDS, and SEM images were taken in the secondary mode. EBSD samples were electrochemically polished with a solution of HNO₃ (15%) and C₂H₅OH (85%) for 1 min at 20 V and -40 °C. Crystal structures were determined by XRD with Cu K α radiation scanning from 30° to 90° degrees in 2 θ at a scanning rate of 5 °/min. XRD analyses were performed using the software MDI Jade 6, which incorporates the database published by the Joint Committee on Powder Diffraction Standards (JCPDS), International Center for Diffraction Data (ICDD) [28]. Phase identification was performed by comparing the intensity and position of measured diffraction peaks with the standard data of the well-known crystal structure in the powder diffraction files (PDFs).

The fraction of σ phase was calculated from the SEM images using the ImageJ software. For each SEM image, the σ precipitates were manually traced, and then the area fraction of σ precipitates was computed by dividing the sum of the σ phase pixels to the total number of pixels in the image. For each sample, at least three SEM images with an area of $60 \times 45 \mu\text{m}^2$ were measured, and the average value was reported. The L1₂ precipitate size calculation was based on measuring the area of each precipitate from the SEM images using the ImageJ software. The area equivalent diameter, d , was calculated using the equation: $d = 2\sqrt{A/\pi}$, where A is the calculated precipitate area. For each sample, at least 300 precipitates from different areas were measured, and the average value was reported.

Thermodynamic calculations were employed to supplement and complement the experimental findings. Thermo-Calc 3.0 with Ni-database (TTNI8) was used to evaluate phase constitutions and transformations. Hardness measurements were performed under an applied load

of 1 kg and a dwelled time of 15 s, and the average hardness from ten different measurements was reported.

3. Results and discussion

3.1 Microstructures of the Al₃Ti₃ alloy

The microstructure and phase relations of the Al₃Ti₃ alloy at 600-900 °C were investigated by XRD, SEM, and EBSD. The XRD patterns of the Al₃Ti₃ alloy after aging for 300 h at 600-900 °C are shown in Fig. 1. At all temperatures, the alloy exhibits three major peaks at 2θ of 44°, 51°, and 75°, which correspond respectively to the (111), (200), and (220) planes of an fcc and/or L1₂ structure. At 700 and 800 °C, three additional minor peaks at 2θ of 42°, 46°, and 47° were observed, which can be indexed as the (410), (420), and (411) planes of a σ phase. These minor peaks are very weak in intensity, suggesting that the volume fraction of σ phase in this alloy may be very close to the detection limit of XRD (approximately 5 vol.%). To illustrate the minor peaks more clearly, we present the XRD data in the sqrt(intensity) in Supplementary Fig. S1a. Representative SEM microstructures of the Al₃Ti₃ alloy after aging for 300 h at 600, 700, 800, and 900 °C are displayed in Fig. 2a-d, respectively. Fine-scale phase separation was observed at all the temperatures studied. The alloy shows lamellar precipitates at 600 °C, whereas a mixed microstructure consisting of lamellar precipitates at grain boundaries and spheroidal particles in grain interiors was observed at 700 and 800 °C. These observations are in agreement with previous reports on fcc/L1₂ M/HEAs, in which lamellar L1₂ precipitates tend to form at grain boundaries and spheroidal L1₂ particles are uniformly distributed in grain interiors^[13,29]. It is known that the L1₂ phase has an ordered simple cubic structure and is coherent with the fcc matrix, exhibiting very similar major diffraction peaks as those of the fcc phase in XRD patterns. Thus, the diffraction

peaks of the (111), (200), and (220) reflections in Fig. 1 should result from both the fcc and L1₂ phases. As the temperature increases to 900 °C, no lamellar precipitates can be observed, and the alloy contains near-cuboidal precipitates at both grain boundaries and grain interiors.

In addition to the L1₂ lamellar precipitates, some discrete blocky precipitates with an irregular shape and dark contrast were observed along grain boundaries at 700 and 800 °C. Their composition and structure were further examined by EDS and EBSD. A representative EDS spectrum of the block precipitates in the 800 °C aged sample is shown in Fig. 2e. The dark-contrasted blocky precipitates are enriched in Cr and Co and depleted in Ni, Al, and Ti. The SEM micrograph and corresponding EBSD phase map of the 800 °C aged sample are shown in Fig. 3. Note that the L1₂ phase can not be differentiated from the fcc matrix by EBSD due to the close relationship between the two crystal structures. The region consisting of the L1₂ precipitates and fcc matrix is indexed as the fcc/L1₂ phase (blue), whereas the blocky precipitates at grain boundaries are determined to be the σ phase (violet). The EDS results, together with the EBSD data, indicate that the blocky precipitates are (Co,Ni)Cr-type σ phases, which is in consistent with the XRD results (cf. Fig. 1). It is noted that the σ phase forms at 700 and 800 °C but not at 600 and 900 °C. To understand the temperature effect on the formation of σ phase, we performed thermodynamic calculations with the Thermo-Calc software to determine how the equilibrium σ volume fraction evolves with temperature (Supplementary Fig. S2a). The calculations predict that the σ solvus temperature is around 950 °C. If one assumes a reasonable uncertainty of several tens of °C in the prediction, the true solvus temperature might be close to 900 °C. In this case, there would be no or little thermodynamic driving force for the formation of σ phase at 900 °C. Thus, the absence of σ phase at this temperature is likely due to the insufficient thermodynamic driving force. As the temperature decreases to 700-800 °C, the calculated volume fraction of σ phase

increases considerably, indicating a substantial increase in the thermodynamic driving force for the σ formation. In addition, the diffusion of solute atoms is efficient at these temperatures. Thus, the σ formation is both thermodynamically and kinetically favorable at these conditions. As a result, the formation of σ phases was observed at 700 and 800 °C. As the temperature decrease to 600 °C, the thermodynamic driving force for the σ formation is further enhanced. However, the growth of σ phase is kinetically inhibited due to the slow diffusion rate at this temperature. Therefore, the formation of σ phase is significantly suppressed, and we did not observe any σ phases at this temperature. From the above analyses, it is apparent that the formation of σ phase depends on the interplay of thermodynamic and kinetic factors, and the σ phase tends to form when both thermodynamic and kinetic factors are favorable.

In addition, it is worthy to point out that the lamellar and spherical $L1_2$ precipitates in Fig. 2a-d are formed through two modes of precipitation, i.e., continuous precipitation (CP) and discontinuous precipitation (DP). CP generally involves the formation of spheroidal nanoparticles within grain interiors, whereas DP occurs at grain boundaries and proceeds inwards by the cellular growth of alternating layers of $L1_2$ precipitates and fcc matrix (with greatly reduced supersaturation) behind a moving grain boundary. Essentially, the DP reaction involves two critical steps, namely heterogeneous grain boundary precipitation and concurrent boundary migration, and the chemical driving force for the growth of discontinuous precipitates results from the chemical potential gradient across the boundary. Thus, any factors affecting the grain boundary characteristics, mobility, or chemistry can have a direct influence on the DP reaction. Generally, a rapid cooling, such as water quenching, can eliminate the grain boundary segregation and suppress, to a certain extent, the DP reaction, whereas a slow cooling (such as air cooling) could result in a redistribution of solute elements near grain boundaries, which may provide a favorable chemical

condition for DP. In this study, to eliminate the formation of discontinuous and continuous precipitates during the cooling process, all samples were cooled by water quenching. Annealing temperature is another important factor having a significant impact on the precipitation mode, because temperature could drastically affect the thermodynamic driving force for precipitation and diffusion of solute atoms. In this study, increasing the temperature from 600 to 900 °C results in the change of precipitate microstructure from DP-dominant to CP-dominant. At 600 °C (Fig. 2a), the bulk diffusion is very limited, which kinetically inhibits the CP reaction, whereas the grain boundary diffusion is still active, which makes the DP reaction faster than the CP reaction [13,29,30]. Moreover, the low temperature leads to a high supersaturation (i.e., a severe composition gradient across the reaction front), which enhances the chemical driving force for the DP reaction. As a result, the DP reaction is dominant at this temperature, leading to the prevailing of lamellar-like discontinuous precipitates throughout the matrix. At 700 and 800 °C, both CP and DP can occur, leading to the mixed microstructure consisting of spherical particles in the grain interiors and lamellar precipitates at grain boundaries (Fig. 2b and c). As the temperature increases to 900 °C, the bulk diffusion is substantially increased; thus, the CP is sufficient to establish a near-equilibrium state, which significantly reduces the composition gradient across the reaction front of DP cells, thereby decreasing the chemical driving force for the DP reaction. In addition, the grain-boundary precipitates formed through the CP reaction tend to have a coarse size and generate a strong pinning effect, which significantly retards the migration of grain boundaries, thereby further inhibiting the DP reaction. Therefore, the CP reaction is dominant at 900 °C, resulting in the formation of a fully CP microstructure, with no observation of DP lamellae at grain boundaries (Fig. 2d). As a result, the microstructure transition from the fully discontinuous lamellar

precipitates (600 °C) to the mixture of discontinuous lamellar and continuous spherical precipitates (700 and 800 °C) and to fully continuous precipitates (900°C) was observed in this alloy.

3.2 Microstructures of the Al₅Ti₅ alloy

The XRD patterns of the Al₅Ti₅ alloy after aging for 300 h at 600-900 °C are shown in Fig. 4, and the data in the sqrt(intensity) is displayed in Supplementary Fig. S1b. As the Al and Ti concentrations increase to 5 at. %, the fcc/L1₂ peaks are still dominating, while the σ phase becomes more obvious. Moreover, the intensity of the σ peaks increases with increased temperature from 600 to 900 °C, suggesting the enhanced precipitation of σ phase at higher temperatures. The SEM micrographs of the Al₅Ti₅ alloy in the 600, 700, 800, and 900 °C aged conditions are illustrated in Fig. 5a-d, respectively. At 600 °C (Fig. 5a), a eutectoid-like structure consisting of dark and bright lamellae was observed. As the temperature increased to 700 °C (Fig. 5b), the eutectoid-like structure coarsens and spheroidizes, and the amount of dark-contrasted regions increases. In addition, in the bright-contrasted lamellae, obvious nano-level precipitates can be observed, which are similar to the discontinuous L1₂ precipitates in the Al₃Ti₃ alloy at 600 °C. With the temperature increasing to 800 °C (Fig. 5c), two categories of precipitates were detected in the Al₅Ti₅ alloy. One category is nanoscale particles that are uniformly distributed in the matrix; they are speculated to be L1₂ precipitates based on previous literature [9-20,26,27,29]. The other is dark-contrasted blocky precipitates with sizes in the micron scale and surrounded by the fcc/L1₂ phase, which are in consistent with the σ precipitates as observed in the Al₃Ti₃ alloy. The EBSD results of the 800 °C aged sample (Fig. 6) confirms that the blocky precipitates are σ phase. Further increasing the temperature to 900 °C leads to the coarsening of both types of precipitates. The average size of L1₂ precipitates increases from approximately 70 nm at 800 °C to 250 nm at 900 °C, which is accompanied by the change of precipitate shape from spheroidal to cuboidal. The

composition of the σ and $L1_2$ precipitates of the Al_5Ti_5 alloy was determined by EDS, and the corresponding spectrums are shown in Fig. 5e. The dark-contrasted blocky precipitates are enriched in Cr and Co and depleted in Ni, Al, and Ti; their composition can be regarded as 55.73Cr-30.83Co-10.92Ni-1.47Ti-1.06Al (at.%), suggesting that the σ phase is of (Co,Ni)Cr-type. The grey-contrasted precipitates are enriched in Ni, Co, Al, and Ti and depleted in Cr; the atom ratio of (Ni + Co) to (Al + Ti) is approximately 3:1, suggesting that they are $(Ni,Co)_3(Al,Ti)$ -type $L1_2$ precipitates. From the above results, it is likely that the σ (dark contrast) and fcc/ $L1_2$ (bright contrast) phases form the eutectoid-like microstructure at low temperatures, and the microstructure coarsens and spheriodizes with increased temperatures, leading to the formation of a hierarchical precipitate microstructure consisting of micron-scale σ precipitates and nanoscale $L1_2$ particles on the fcc matrix.

To understand the temporal evolution of the $L1_2$ and σ precipitates with aging time, we conducted systematic aging experiments on the Al_5Ti_5 alloy at 900 °C for various periods of time from 1 to 300 h, and the SEM micrographs of the alloy in the different aging conditions are presented in Fig. 7. After annealing for 1 h (Fig. 7a), a high number density of $L1_2$ nanoparticles is uniformly distributed in the fcc matrix, whereas a small amount of needle-like σ precipitates was occasionally observed in the grain interior, suggesting that the precipitation of $L1_2$ nanoparticles occur earlier than that of σ needles. As the aging time increases to 10 h (Fig. 7b), the volume fraction of needle-like σ precipitates increases, and additional elliptical σ precipitates were frequently observed. Moreover, the periphery of the elliptical σ precipitates is decorated by $L1_2$ precipitates with irregular morphologies. With the aging time increasing to 50 h (Fig. 7c), the volume fraction and size of σ precipitates increase progressively. The needle-like σ precipitates coarsen to a rod-like shape after aging for 100 h (Fig. 7d). Further increasing the aging time to 300

h results in a morphology change of σ precipitates from the rod-like to blocky shape (Fig. 7e), which is likely to be due to the coarsening effect. Meanwhile, the irregular $L1_2$ precipitates decorated at the periphery of σ precipitates are found to coarsen to the micron scale and become discrete. Therefore, the temporal evolution results indicate that there are two types of $L1_2$ precipitates in this alloy. One is the homogeneous precipitation of $L1_2$ nanoparticles in the fcc matrix, and their morphology transforms from spheroidal to cuboidal with increased aging time. The other is the heterogeneous precipitation of $L1_2$ precipitates at the σ /matrix interface, and these precipitates exhibit irregular morphologies and coarse sizes. Because the σ precipitates are enriched in Cr and Co and depleted in Ni, Al, and Ti, their formation consumes Cr and Co, leaving the matrix enriched in Ni, Al, and Ti. These three elements are $L1_2$ forming elements, and their enrichment can promote the formation of $L1_2$ precipitates. Moreover, the σ /matrix interface can act as preferred nucleation sites for heterogeneous nucleation. As a result, a high-volume fraction of coarse-sized $L1_2$ precipitates was observed surrounding the σ precipitates.

In addition, increasing aging time also results in coarsening and morphological changes of $L1_2$ precipitates in grain interiors. The average diameter of nanoscale $L1_2$ precipitates increases from approximately 40 nm at 1 h to 100 nm at 50 h and to 250 nm at 300 h, and their shape changes from spheroidal at 1 h to near-cuboidal at 50 h and to cuboidal at 300 h. Essentially, the equilibrium shape of the $L1_2$ precipitates is determined by minimizing the sum of interfacial and elastic strain energies. The interfacial energy scales with the surface area of the precipitates, whereas the elastic strain energy scales with the volume of the precipitates. Thus, the shape changes may occur with a change in the precipitate size. When the precipitates are small, the interfacial energy would contribute more to the overall shape because the area to volume ratio is large; thus, the precipitates tend to have a spheroidal shape that minimizes the interfacial energy. During the coarsening

process, the precipitates depart from a spheroidal morphology because of the lattice misfit which leads to an increase in the elastic strain energy. Previous studies demonstrated that in HEAs the L_{12} precipitates have a coherent cube-on-cube relationship with the fcc matrix, similar as that in Ni-based superalloys^[31,32]. Thus, the coarse L_{12} precipitates tend to have a cuboidal morphology and align along the cubic directions of the fcc matrix. Therefore, we observed that as the aging time increases, the L_{12} precipitates change from a spheroidal shape to a cuboidal morphology.

3.3 Microstructures of the Al_7Ti_7 alloy

The XRD patterns of the Al_7Ti_7 alloy after aging for 300 h at 600, 700, 800, and 900 °C are shown in Fig. 8, and the data in the $\sqrt{\text{intensity}}$ is displayed in Supplementary Fig. S1c. It is evident that the fcc/ L_{12} and σ phases are prevailing at all the temperatures studied. Intriguing, additional minor peaks corresponding to a L_{21} -Heusler phase were also detected, suggesting that increasing the Al and Ti concentrations induces the precipitation of L_{21} phases. The SEM microstructures of the Al_7Ti_7 alloy at 600, 700, 800, and 900 °C are displayed in Fig. 9a-d, respectively. The alloy exhibits a network-like structure containing multiple phases (L_{12} , σ and L_{21} phase), and this network-like structure with raised and recessed regions coarsens from approximately 200 nm at 600 °C to a few microns at 900 °C. The EDS results (Fig. 9e) reveals that the alloy has three phases. The recessed region is enriched in Cr and Co and depleted in Ni, Al, and Ti, which is similar to the σ -(Co,Ni)Cr phase as observed in the Al_5Ti_5 alloy. The raised region with grey contrast has a (Ni + Co):(Al + Ti) ratio of approximately 3:1, which is in agreement with the composition of L_{12} -(Ni,Co)₃(Al,Ti) phase. Thus, the peaks observed at 2θ of 44°, 51°, and 75° in the XRD patterns in Fig. 8 are from the ordered L_{12} phase. By contrast, the raised region with dark contrast has a (Ni + Co):(Al + Ti) ratio of approximately 2:1, which is in accordance with the composition of L_{21} -(Ni,Co)₂AlTi phase. It is noted that the L_{21} phase has a doubly ordered

bcc structure, whereas the $L1_2$ phase has an ordered simple cubic structure; thus, the two phases can be differentiated via EBSD. The SEM micrograph and corresponding EBSD map of the Al_7Ti_7 alloy at 900 °C are shown in Fig. 10. It is evident that the Al_7Ti_7 alloy consists of three phases, i.e., the $L1_2$ (blue), σ (violet), and $L2_1$ (yellow) phases. Noticeably, the $L2_1$ phase is found to be adjacent to or surrounded by the $L1_2$ phase, especially the coarse-sized one.

The σ phase compositions in the Al_3Ti_3 , Al_5Ti_5 , and Al_7Ti_7 alloys are very similar, with a minor difference in the Cr concentration. The Cr concentration of the σ phase increases slightly from 52.0 at.% in the Al_3Ti_3 alloy to 55.7 at.% in the Al_5Ti_5 alloy and then decreases to 53.8 at.% in the Al_7Ti_7 alloy. A possible reason for the change in the Cr concentration is a combination of two contrary factors: on the one hand, as previous studies have indicated, increasing the Al and Ti concentrations promote the formation of σ phase and enhances the partitioning of Cr to the σ phase [33]; on the other hand, increasing the Al and Ti concentrations directly decreases the Cr concentration in the overall composition, which diminishes the partitioning of Cr to the σ phase. The precipitation behavior of the σ phase in the three alloys are different in the amount, location, and morphology. The volume fraction of the σ phase increases from approximately 0 in the Al_3Ti_3 alloy to 20 % in the Al_5Ti_5 alloy and to 35 % in the Al_7Ti_7 alloy, which can be ascribed to the high chemical driving force for the σ precipitation. During the solutionizing treatment at 1150 °C, the three alloys form an fcc solid solution. Upon water quenching, the three alloys are expected to retain a supersaturated solid solution. The SEM micrographs in the pre-aged condition (Supplementary Fig. S3) reveal that the three alloys exhibit a fully recrystallized grain structure comprising equiaxed grains with average sizes of 20-30 μm , and there is no evidence for phase decomposition or precipitation in the as-quenched samples. In the Co-Cr-Ni-Al-Ti system, Cr and Co tend to form sigma phase, whereas Ni, Al, and Ti tend to precipitate as $Ni_3(Al,Ti)$ precipitates.

Thus, upon annealing the metastable supersaturated solid solution at intermediate temperatures, the sigma and L₁₂ phases precipitate out from the fcc matrix. In addition, increasing the Al and Ti concentrations results in an increase in the volume fraction of L₁₂-(Ni,Co)₃(Al,Ti) precipitates, which makes the remaining region enriched in Cr, thereby increasing the volume fraction of the Cr-enriched σ phase. Furthermore, unlike the Al₃Ti₃ alloy that has a small amount of σ precipitates at grain boundaries only, the Al₅Ti₅ and Al₇Ti₇ alloys show the precipitation of σ precipitates at both grain boundaries and grain interiors, and their morphology changes from a lamellar to blocky shape possibly due to the coarsening and spheroidizing effect.

To quantitatively understand the effect of Al and Ti concentrations on the L₁₂ and σ precipitation behavior, thermodynamic calculations were performed by using the Thermo-Calc software. The calculated volume fractions of the L₁₂ and σ phases are displayed in Fig. 11, and the complete phase diagrams are shown Fig. S2. The measured volume fraction of L₁₂ phase in the Al₃Ti₃, Al₅Ti₅, and Al₇Ti₇ alloys at 900 °C are 13%, 34%, and 55%, respectively, which are comparable to the calculated values at the same temperature, 18%, 38%, and 57%, respectively. For the σ phase, the measured volume fraction in the Al₃Ti₃, Al₅Ti₅, and Al₇Ti₇ alloys at 900 °C are 0, 20%, and 35%, respectively, which are also close to the calculated values, 7%, 29%, and 43%, respectively. Therefore, the experimental results are in good agreement with the calculation ones in terms of the L₁₂ and σ phases within experimental uncertainties. However, it is worthy to point out that we observed a considerable amount of L₂₁ precipitates in the Al₇Ti₇ alloy, which was not predicted by the calculations. In fact, the precipitation of L₂₁ phases in L₁₂-strengthened M/HEA were frequently reported in previous studies. Choudhuri et al. [34] calculated the formation energy of the L₁₂-Ni₃Al and L₂₁-Ni₂AlTi phases through first-principles calculations, and their results revealed that the L₂₁ phase is energetically more stable than the L₁₂ phase and high Ti

concentrations promote the transformation of the $L1_2$ to $L2_1$ phase. In addition, Yang et al. [35] reported that higher Ti and Al supersaturations thermodynamically destabilize the $L1_2$ precipitates and induce the formation of $L2_1$ Heusler phase. Therefore, it is possible that the high Al and Ti concentration (both 7 at.%) induces high Ti and Al supersaturations, leading to the formation of $L2_1$ precipitates in the Al_7Ti_7 alloy (cf. Fig. 10).

3.4 Mechanical properties

The mechanical properties of these alloys were preliminarily analyzed in terms of hardness. The hardness profiles of the Al_3Ti_3 , Al_5Ti_5 , and Al_7Ti_7 alloys are displayed in Fig. 12 as a function of aging temperature. The results indicate that at all temperatures studied, the hardness of the alloys is in the order (lowest to highest): Al_3Ti_3 , Al_5Ti_5 , and Al_7Ti_7 ; this is likely to be due to the increased volume fraction of the σ , $L1_2$, and $L2_1$ phases in the alloys. The volume fraction of the σ phase increases from 0 in the Al_3Ti_3 alloy to 20% in the Al_5Ti_5 alloy and to 35% in the Al_7Ti_7 alloy at 900 °C, whereas that of the $L1_2$ phase increases from 13% in the Al_3Ti_3 alloy to 34% in the Al_5Ti_5 alloy and to 55% in the Al_7Ti_7 alloy. Moreover, the Al_7Ti_7 alloy reveals the formation of a considerable amount of $L2_1$ phase, which was not observed in the Al_3Ti_3 and Al_5Ti_5 alloys. It is known that the σ , $L1_2$, and $L2_1$ phases are much harder than the fcc phase; thus, it is reasonable that increasing the volume fraction of the σ , $L1_2$, and $L2_1$ phases results in a high hardness. In addition, it was observed that for all the alloys, the hardness decreases monotonously with increasing temperature, which is possibly due to the coarsening of the σ , $L1_2$, and $L2_1$ phases. Lastly, it is worthy of note that the Al_5Ti_5 and Al_7Ti_7 alloys exhibit high hardness values of above 600 HV after aging at 600-800 °C, making them promising candidates for wear resistant applications.

4. Conclusions

Through the systematic investigation of the effects of alloying additions and aging temperature on the phase relations and precipitate microstructure of the $(\text{CoCrNi})_{100-2x}(\text{AlTi})_x$ MEAs at intermediate temperatures, the following conclusions are drawn:

1. EDS reveals that the L_{12} precipitates are enriched in Ni, Al, and Ti, whereas the σ precipitates are enriched in Co and Cr. Increasing the Al and Ti additions enhances the chemical driving force for the formation of L_{12} precipitates and promotes the destabilization of supersaturated fcc into L_{12} and σ phases. The dominating phases change from fcc + L_{12} in the Al_3Ti_3 alloy to fcc + L_{12} + σ in the Al_5Ti_5 alloy and to L_{12} + σ + L_{21} in the Al_7Ti_7 alloy. In addition, the σ phase forms at 700 and 800 °C but not at 600 and 900 °C, which is a result of the interplay between thermodynamic and kinetic factors.

2. The σ , fcc, and L_{12} phases form a lamellar microstructure at low temperatures, and increasing the temperature induces the coarsening and spheroidizing of the microstructure, leading to the change of precipitate morphology from lamellar to granular structures. In particular, the L_{12} precipitates are formed through two competitive modes of precipitation, i.e., CP and DP. Increasing the temperature from 600 to 900 °C results in the change of precipitate microstructure from DP-dominant to CP-dominant.

3. There are two types of L_{12} precipitates in the Al_5Ti_5 alloy. One is the homogeneous precipitation of L_{12} nanoparticles in the fcc matrix, whose morphology changes from spheroidal to cuboidal with increased aging time, and the other is the heterogeneous precipitation of L_{12} precipitates at the σ /matrix interface, which exhibit irregular morphologies and coarse sizes. In addition, increasing aging time also results in coarsening and morphological changes of L_{12} precipitates in grain interiors. As the aging time increases, the L_{12} precipitates change from a

spheroidal shape to a cuboidal morphology, which is a result of the competition between interfacial and elastic energies.

4. The hardness of the alloys is in the order (lowest to highest): Al_3Ti_3 , Al_5Ti_5 , and Al_7Ti_7 at the temperatures studied, which is likely to be due to the increased volume fraction of the σ , L_{12} , and L_{21} phases. Particularly, the Al_5Ti_5 and Al_7Ti_7 alloys exhibit high hardness values of above 600 HV after aging at 600-800 °C, making them promising candidates for wear resistant applications.

Acknowledgements

This research was supported by the Early Career Scheme from the Research Grants Council of Hong Kong (25202719), State Key Laboratory for Advanced Metals and Materials Open Fund (2021-ZD04), Guangzhou International Science & Technology Cooperation Program (201907010026), and PolyU internal funds (P0009738, P0000538, and P0013994).

References

1. J.W. Yeh, S.K. Chen, S.J. Lin, J.Y. Gan, T.S. Chin, T.T. Shun, C.H. Tsau, S.Y. Chang, Nanostructured high-entropy alloys with multiple principal elements: novel alloy design concepts and outcomes, *Adv. Eng. Mater.*, 2004, 6(5), 299-303.
2. M.C. Gao, Progress in high-entropy alloys, *JOM*, 2014, 66(10), 1964-1965.
3. Y. Zhang, T.T. Zuo, Z. Tang, M.C. Gao, K.A. Dahmen, P.K. Liaw, Z.P. Lu, Microstructures and properties of high-entropy alloys, *Prog. Mater. Sci.*, 2014, 61 1-93.
4. D.B. Miracle, O.N. Senkov, A critical review of high entropy alloys and related concepts, *Acta Mater.*, 2017, 122 448-511.
5. E.P. George, D. Raabe, R.O. Ritchie, High-entropy alloys, *Nat. Rev. Mater.*, 2019, 4(8), 515-534.

6. Q. Lin, J. Liu, X. An, H. Wang, Y. Zhang, X. Liao, Cryogenic-deformation-induced phase transformation in an FeCoCrNi high-entropy alloy, *Mater. Res. Lett.*, 2018, 6(4), 236-243.
7. D. Wei, X. Li, S. Schönecker, J. Jiang, W.-M. Choi, B.-J. Lee, H.S. Kim, A. Chiba, H. Kato, Development of strong and ductile metastable face-centered cubic single-phase high-entropy alloys, *Acta Mater.*, 2019, 181 318-330.
8. Y. Ma, J. Hao, J. Jie, Q. Wang, C. Dong, Coherent precipitation and strengthening in a dual-phase AlNi₂Co₂Fe_{1.5}Cr_{1.5} high-entropy alloy, *Mater. Sci. Eng., A*, 2019, 764 138241.
9. B. Gwalani, D. Choudhuri, V. Soni, Y. Ren, M. Styles, J. Hwang, S. Nam, H. Ryu, S.H. Hong, R. Banerjee, Cu assisted stabilization and nucleation of L₁₂ precipitates in Al_{0.3}CuFeCrNi₂ fcc-based high entropy alloy, *Acta Mater.*, 2017, 129 170-182.
10. S. Antonov, M. Dettois, S. Tin, Design of novel precipitate-strengthened Al-Co-Cr-Fe-Nb-Ni high-entropy superalloys, *Metall. Mater. Trans. A*, 2018, 49(1), 305-320.
11. Z. Wang, W. Zhou, L. Fu, J. Wang, R. Luo, X. Han, B. Chen, X. Wang, Effect of coherent L₁₂ nanoprecipitates on the tensile behavior of a fcc-based high-entropy alloy, *Mater. Sci. Eng., A*, 2017, 696 503-510.
12. Y.-J. Chang, A.-C. Yeh, The formation of cellular precipitate and its effect on the tensile properties of a precipitation strengthened high entropy alloy, *Mater. Chem. Phys.*, 2018, 210 111-119.
13. Y. Zhao, T. Yang, Y. Tong, J. Wang, J. Luan, Z. Jiao, D. Chen, Y. Yang, A. Hu, C. Liu, Heterogeneous precipitation behavior and stacking-fault-mediated deformation in a CoCrNi-based medium-entropy alloy, *Acta Mater.*, 2017, 138 72-82.
14. T.-K. Tsao, A.-C. Yeh, C.-M. Kuo, K. Kakehi, H. Murakami, J.-W. Yeh, S.-R. Jian, The High Temperature Tensile and Creep Behaviors of High Entropy Superalloy, *Sci. Rep.*, 2017, 7(1), 12658.
15. M.-H. Tsai, H. Yuan, G. Cheng, W. Xu, K.-Y. Tsai, C.-W. Tsai, W.W. Jian, C.-C. Juan, W.-J. Shen, M.-H. Chuang, Morphology, structure and composition of precipitates in Al_{0.3}CoCrCu_{0.5}FeNi high-entropy alloy, *Intermetallics*, 2013, 32 329-336.
16. X. Xu, P. Liu, S. Guo, A. Hirata, T. Fujita, T. Nieh, C. Liu, M. Chen, Nanoscale phase separation in a fcc-based CoCrCuFeNiAl_{0.5} high-entropy alloy, *Acta Mater.*, 2015, 84 145-152.

17. A.M. Manzoni, S. Singh, H.M. Daoud, R. Popp, R. Völkl, U. Glatzel, N. Wanderka, On the path to optimizing the Al-Co-Cr-Cu-Fe-Ni-Ti high entropy alloy family for high temperature applications, *Entropy*, 2016, 18(4), 104.
18. S. Guo, Phase selection rules for cast high entropy alloys: an overview, *Mater. Sci. Technol.*, 2015, 31(10), 1223-1230.
19. J. He, H. Wang, H. Huang, X. Xu, M. Chen, Y. Wu, X. Liu, T. Nieh, K. An, Z. Lu, A precipitation-hardened high-entropy alloy with outstanding tensile properties, *Acta Mater.*, 2016, 102 187-196.
20. Y. Zhao, H. Chen, Z. Lu, T. Nieh, Thermal stability and coarsening of coherent particles in a precipitation-hardened (NiCoFeCr)₉₄Ti₂Al₄ high-entropy alloy, *Acta Mater.*, 2018, 147 184-194.
21. Y. Wu, F. Zhang, X. Yuan, H. Huang, X. Wen, Y. Wang, M. Zhang, H. Wu, X. Liu, H. Wang, Short-range ordering and its effects on mechanical properties of high-entropy alloys, *J. Mater. Sci. Technol.*, 2021, 62 214-220.
22. B. Gwalani, V. Soni, D. Choudhuri, M. Lee, J. Hwang, S. Nam, H. Ryu, S.H. Hong, R. Banerjee, Stability of ordered L1₂ and B2 precipitates in face centered cubic based high entropy alloys-Al_{0.3}CoFeCrNi and Al_{0.3}CuFeCrNi₂, *Scr. Mater.*, 2016, 123 130-134.
23. T. Borkar, B. Gwalani, D. Choudhuri, C. Mikler, C. Yannetta, X. Chen, R.V. Ramanujan, M. Styles, M. Gibson, R. Banerjee, A combinatorial assessment of Al_xCrCuFeNi₂ (0 < x < 1.5) complex concentrated alloys: Microstructure, microhardness, and magnetic properties, *Acta Mater.*, 2016, 116 63-76.
24. C.-W. Lin, M.-H. Tsai, C.-W. Tsai, J.-W. Yeh, S.-K. Chen, Microstructure and aging behaviour of Al₅Cr₃₂Fe₃₅Ni₂₂Ti₆ high entropy alloy, *Mater. Sci. Technol.*, 2015, 31(10), 1165-1170.
25. X.H. Du, W.P. Li, H.T. Chang, T. Yang, G.S. Duan, B.L. Wu, J.C. Huang, F.R. Chen, C.T. Liu, W.S. Chuang, Y. Lu, M.L. Sui, E.W. Huang, Dual heterogeneous structures lead to ultrahigh strength and uniform ductility in a Co-Cr-Ni medium-entropy alloy, *Nat. Commun.*, 2020, 11(1), 2390.
26. Y. Zhao, T. Yang, B. Han, J. Luan, D. Chen, W. Kai, C.T. Liu, J.-j. Kai, Exceptional nanostructure stability and its origins in the CoCrNi-based precipitation-strengthened medium-entropy alloy, *Mater. Res. Lett.*, 2019, 7(4), 152-158.

27. N. An, Y. Sun, Y. Wu, J. Tian, Z. Li, Q. Li, J. Chen, X. Hui, High temperature strengthening via nanoscale precipitation in wrought CoCrNi-based medium-entropy alloys, *Mater. Sci. Eng., A*, 2020, 798 140213.
28. R. Jenkins, Profile Data Acquisition for the JCPDS-ICDD Database, *Aust. J. Phys.*, 1988, 41(2), 145-154.
29. L. Fan, T. Yang, J. Luan, Z. Jiao, Control of discontinuous and continuous precipitation of γ' -strengthened high-entropy alloys through nanoscale Nb segregation and partitioning, *J. Alloys Compd.*, 2020, 832 154903.
30. L. Fan, T. Yang, Y. Zhao, J. Luan, G. Zhou, H. Wang, Z. Jiao, C.-T. Liu, Ultrahigh strength and ductility in newly developed materials with coherent nanolamellar architectures, *Nat. Commun.*, 2020, 11(1), 1-8.
31. M. Doi, T. Miyazaki, T. Wakatsuki, The effect of elastic interaction energy on the morphology of γ' precipitates in nickel-based alloys, *Materials Science and Engineering*, 1984, 67(2), 247-253.
32. R. Wagner, R. Kampmann, P.W. Voorhees, Homogeneous second-phase precipitation, *Phase transformations in materials*, 2001, 5 309.
33. A. Wilson, Formation and effect of topologically close-packed phases in nickel-base superalloys, *Mater. Sci. Technol.*, 2017, 33(9), 1108-1118.
34. D. Choudhuri, T. Alam, T. Borkar, B. Gwalani, A. Mantri, S. Srinivasan, M. Gibson, R. Banerjee, Formation of a Huesler-like $L2_1$ phase in a CoCrCuFeNiAlTi high-entropy alloy, *Scr. Mater.*, 2015, 100 36-39.
35. T. Yang, Y. Zhao, L. Fan, J. Wei, J. Luan, W. Liu, C. Wang, Z. Jiao, J. Kai, C. Liu, Control of nanoscale precipitation and elimination of intermediate-temperature embrittlement in multicomponent high-entropy alloys, *Acta Mater.*, 2020, 189 47-59.

Figure captions

Fig. 1. XRD profiles of the Al_3Ti_3 alloy at 600-900 °C.

Fig. 2. Secondary electron SEM microstructures of the Al_3Ti_3 alloy at (a) 600 °C, (b) 700 °C, (c) 800 °C, and (d) 900 °C, and (e) EDS spectrum of the σ phase in the 800 °C aged sample.

Fig. 3. (a) Secondary electron SEM micrograph and (b) corresponding EBSD phase map of the Al_3Ti_3 alloy at 800 °C.

Fig. 4. XRD profiles of the Al_5Ti_5 alloy at 600-900 °C.

Fig. 5. Secondary electron SEM microstructures of the Al_5Ti_5 alloy at (a) 600 °C, (b) 700 °C, (c) 800 °C, and (d) 900 °C, and (e) EDS spectrum of the σ and L_{12} phases in the 900 °C aged sample.

Fig. 6. (a) Secondary electron SEM micrograph and (b) corresponding EBSD phase map of the Al_5Ti_5 alloy at 800 °C.

Fig. 7. Secondary electron SEM microstructures of the Al_5Ti_5 alloy after aging for different times at 900 °C: (a) 1 h, (b) 10 h, (c) 50 h, (d) 100 h, and (e) 300 h.

Fig. 8. XRD profiles of the Al_7Ti_7 alloy at 600-900 °C.

Fig. 9. Secondary electron SEM microstructures of the Al_7Ti_7 alloy at (a) 600 °C, (b) 700 °C, (c) 800 °C, and (d) 900 °C, and (e) EDS spectrum of the σ , L_{12} , and L_{21} phases in the 900 °C aged sample.

Fig. 10. (a) Secondary electron SEM micrograph and (b) corresponding EBSD phase map of the Al_7Ti_7 alloy at 800 °C.

Fig. 11. Calculated volume fractions of (a) $L1_2$ and (b) σ phases as a function of temperature for the Al_3Ti_3 , Al_5Ti_5 , and Al_7Ti_7 alloys.

Fig. 12. Microhardness of the Al_3Ti_3 , Al_5Ti_5 , and Al_7Ti_7 alloys as a function of aging temperature.

Fig. 1

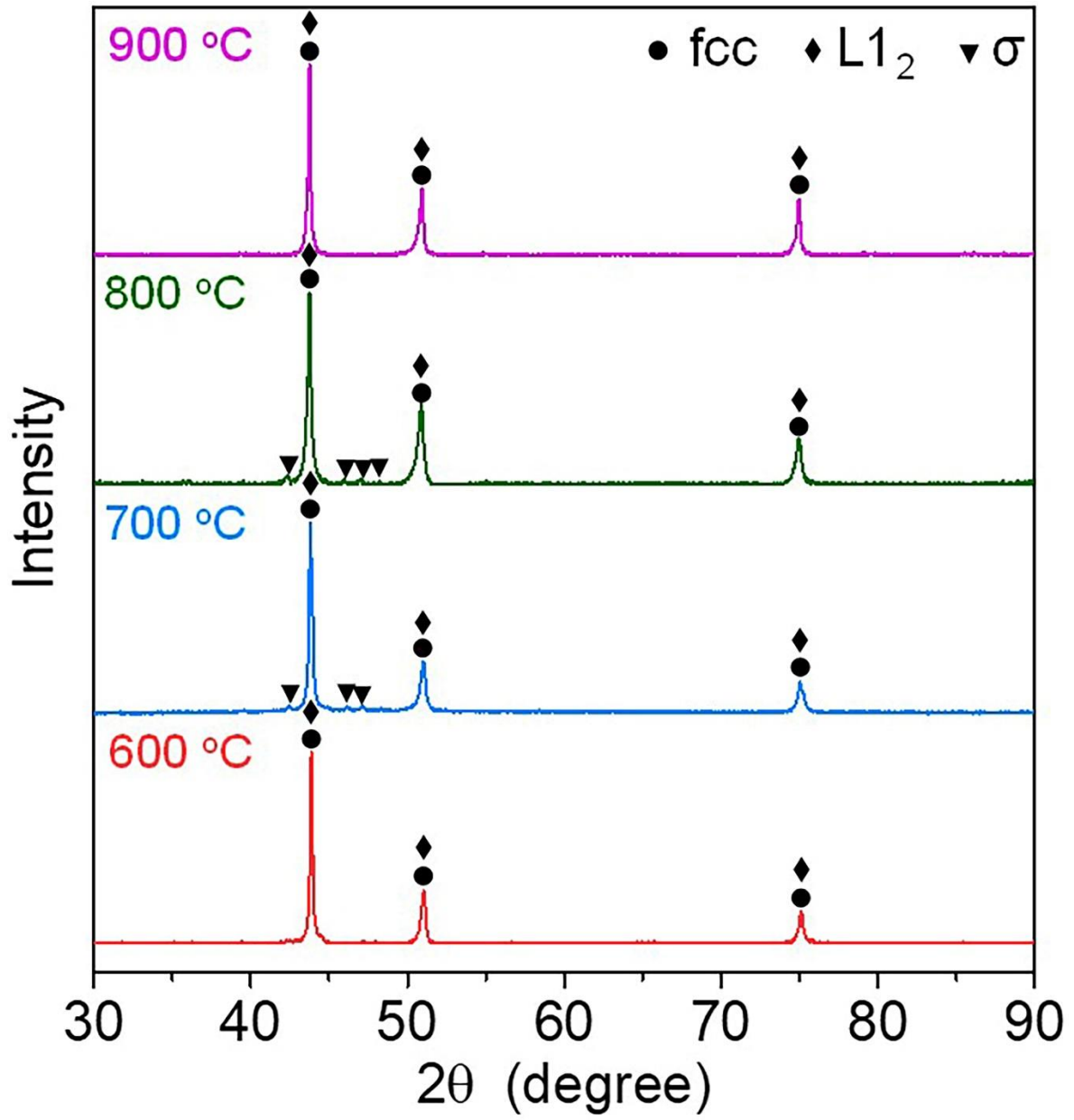


Fig. 2

Al₃Ti₃ alloy

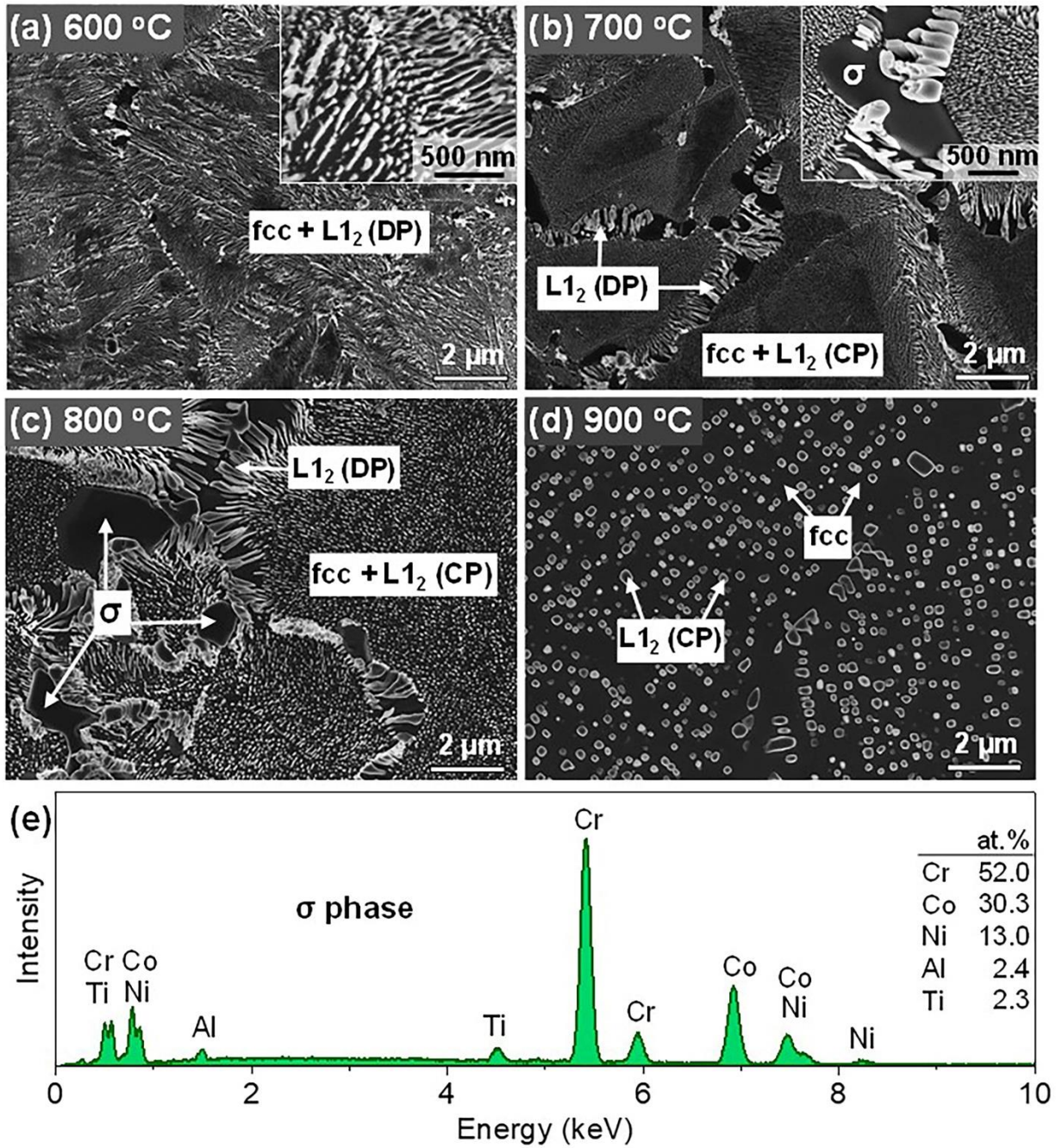


Fig. 3

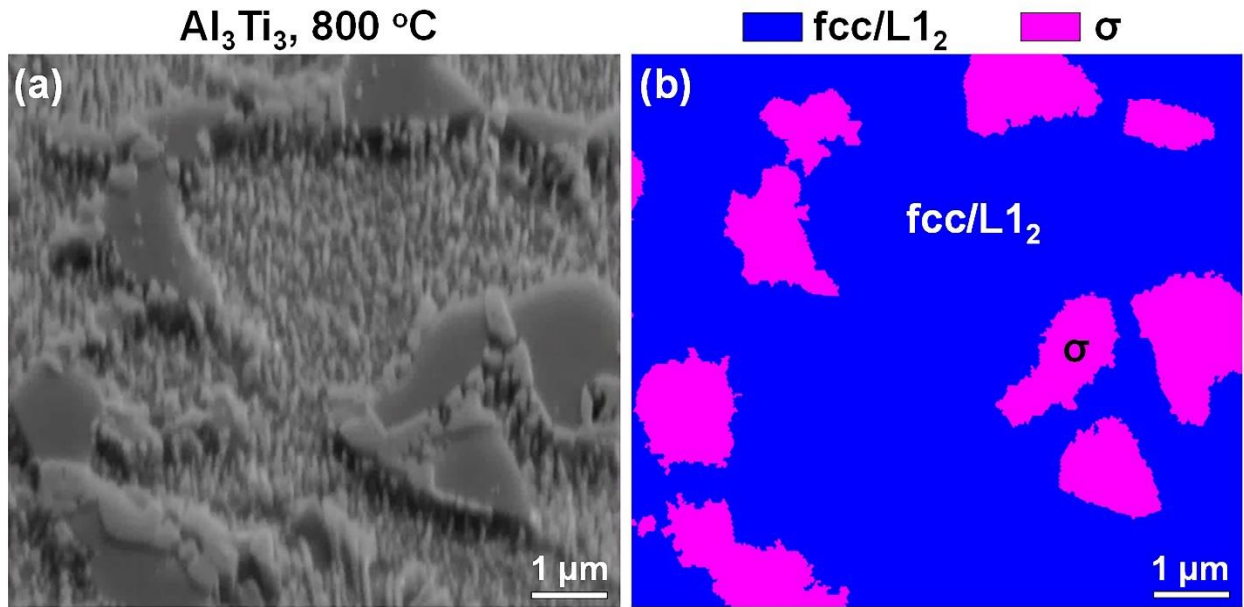


Fig. 4

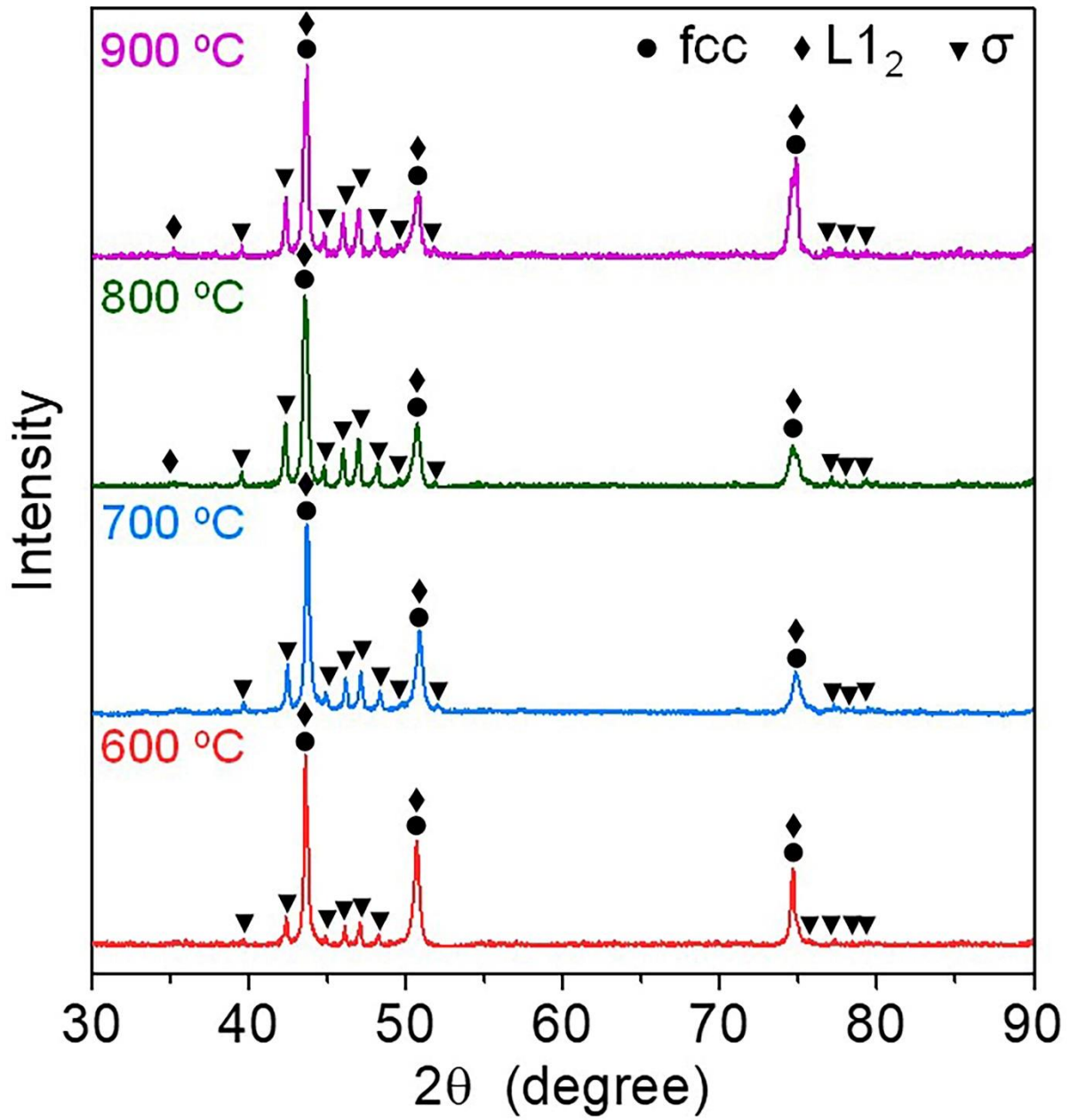


Fig. 5

Al₅Ti₅ alloy

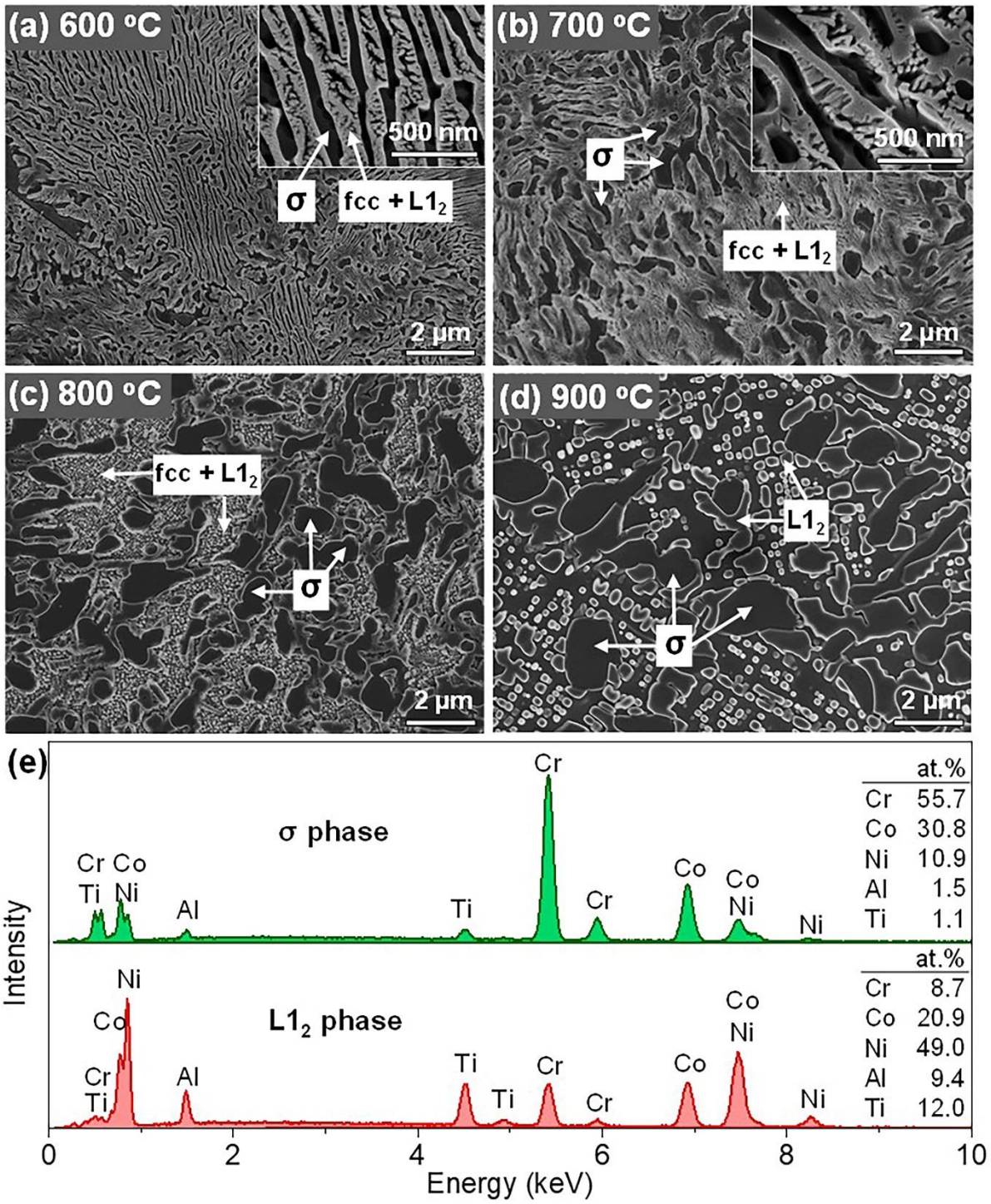


Fig. 6

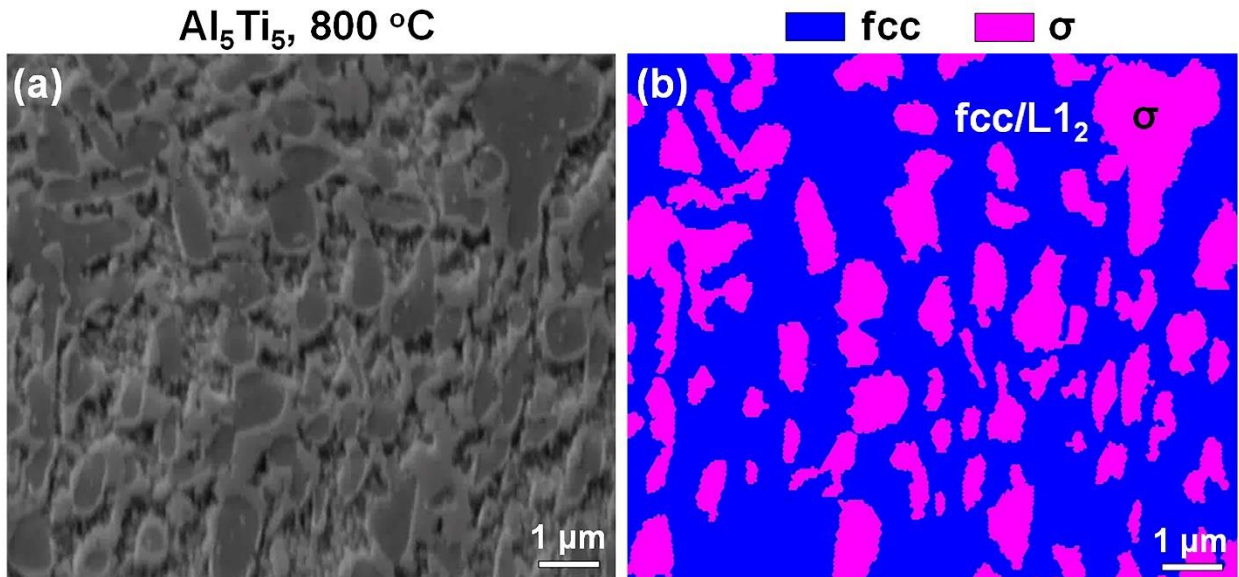


Fig. 7

Al_5Ti_5 , 900 °C

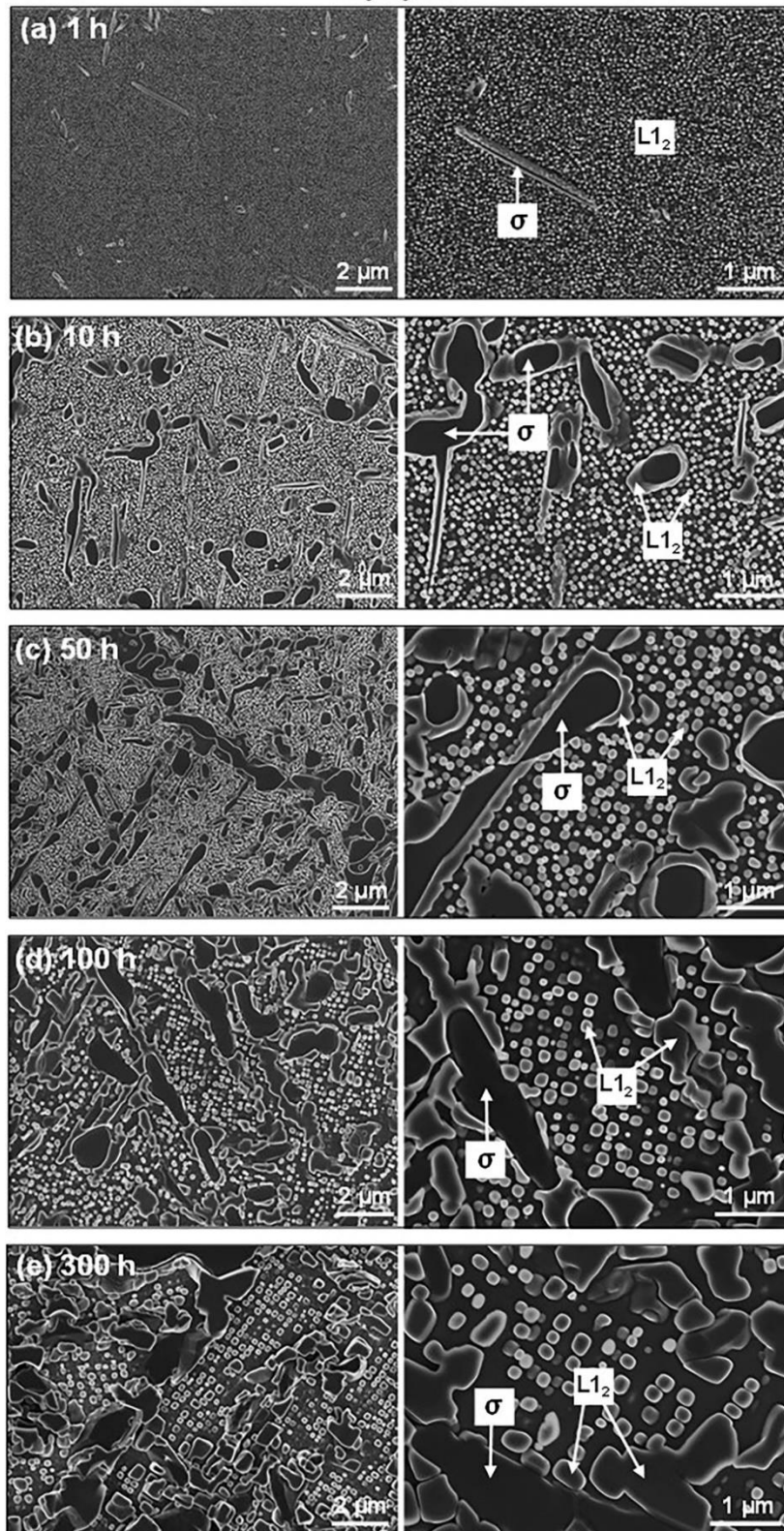


Fig. 8

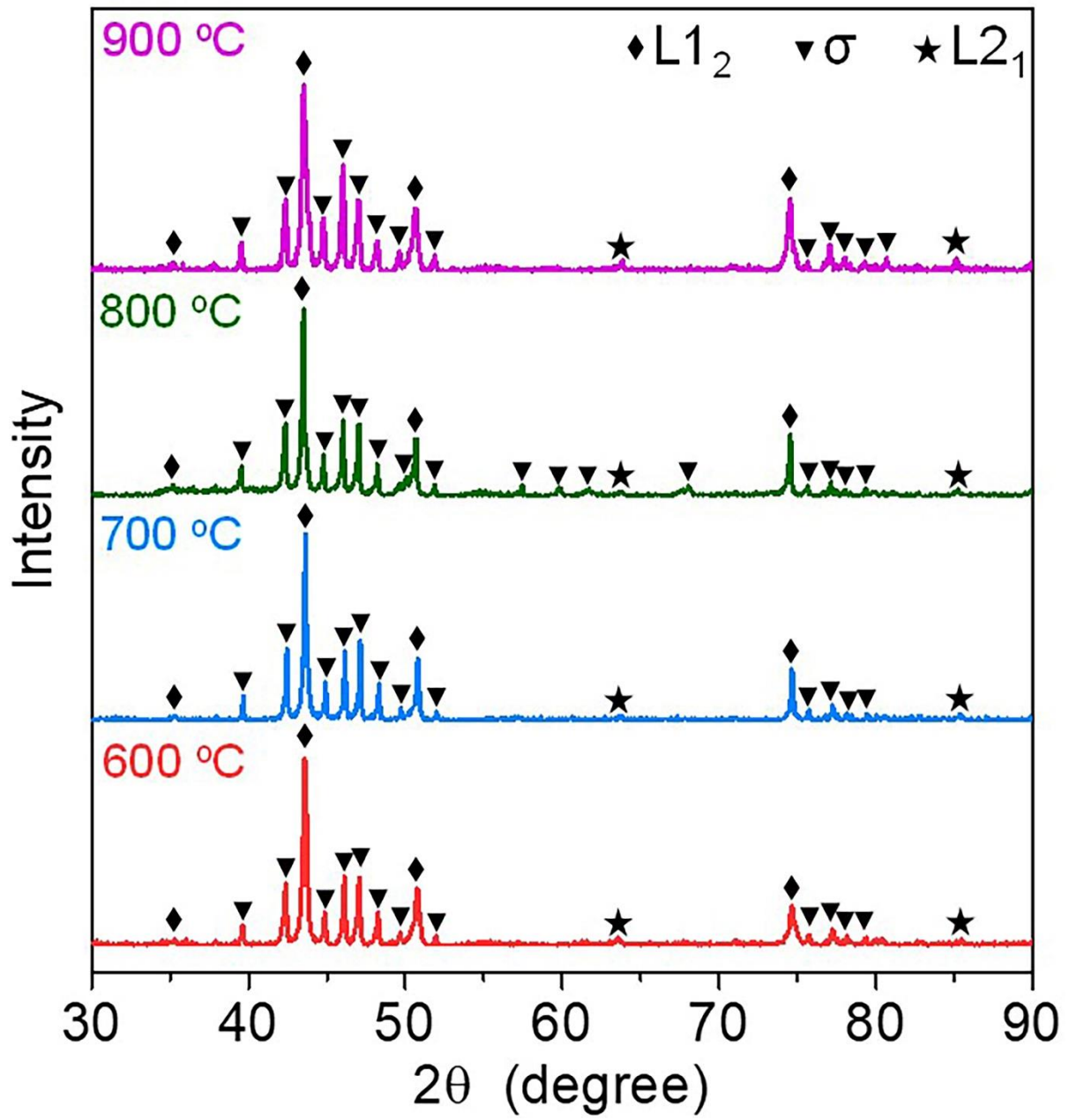


Fig. 9

Al₇Ti₇ alloy

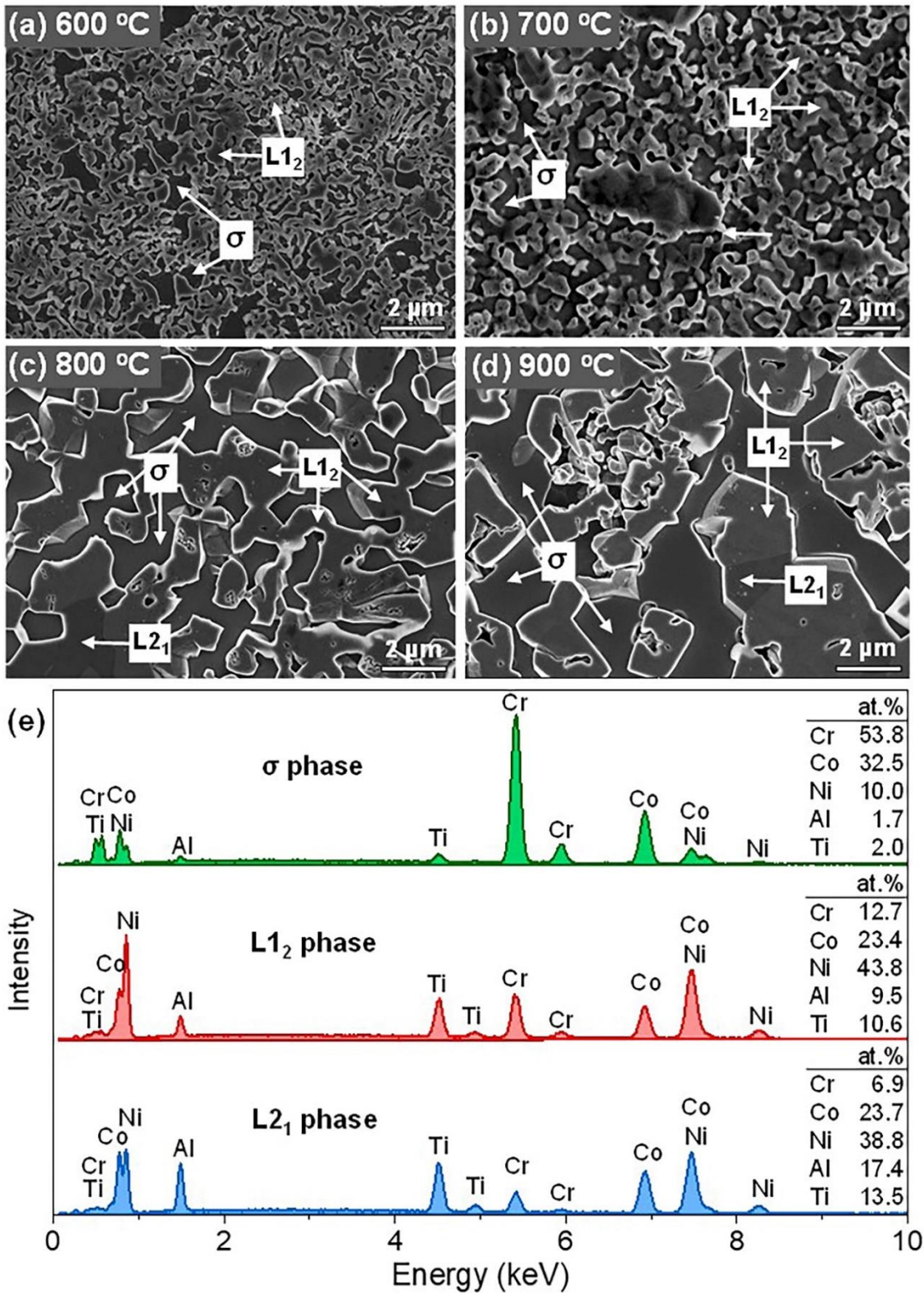


Fig. 10

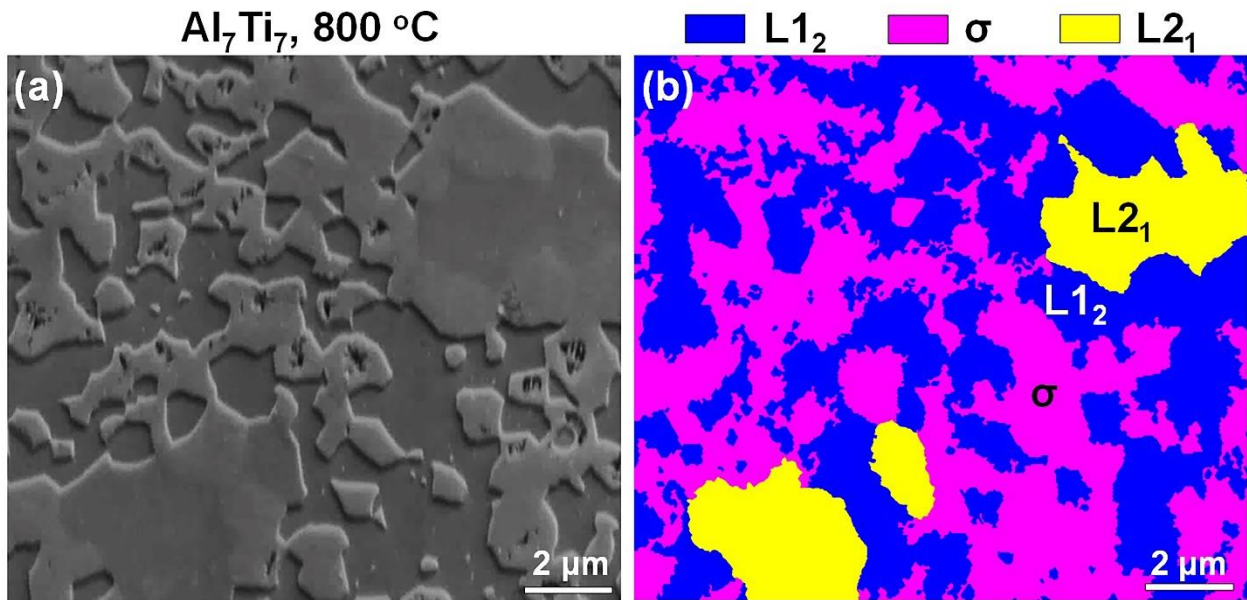


Fig. 11

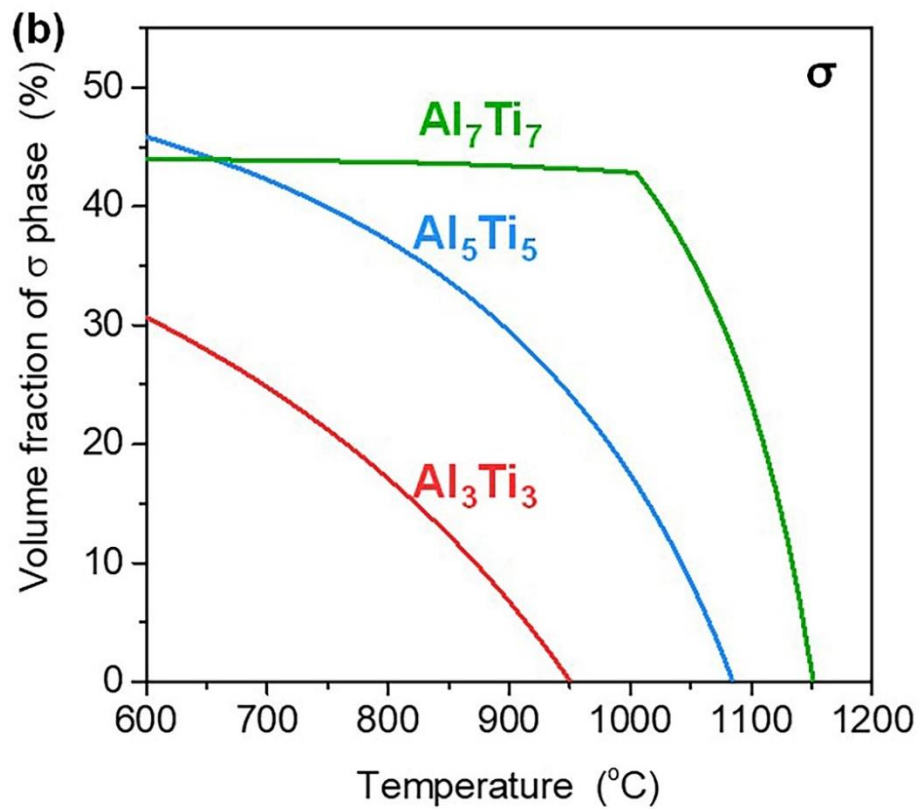
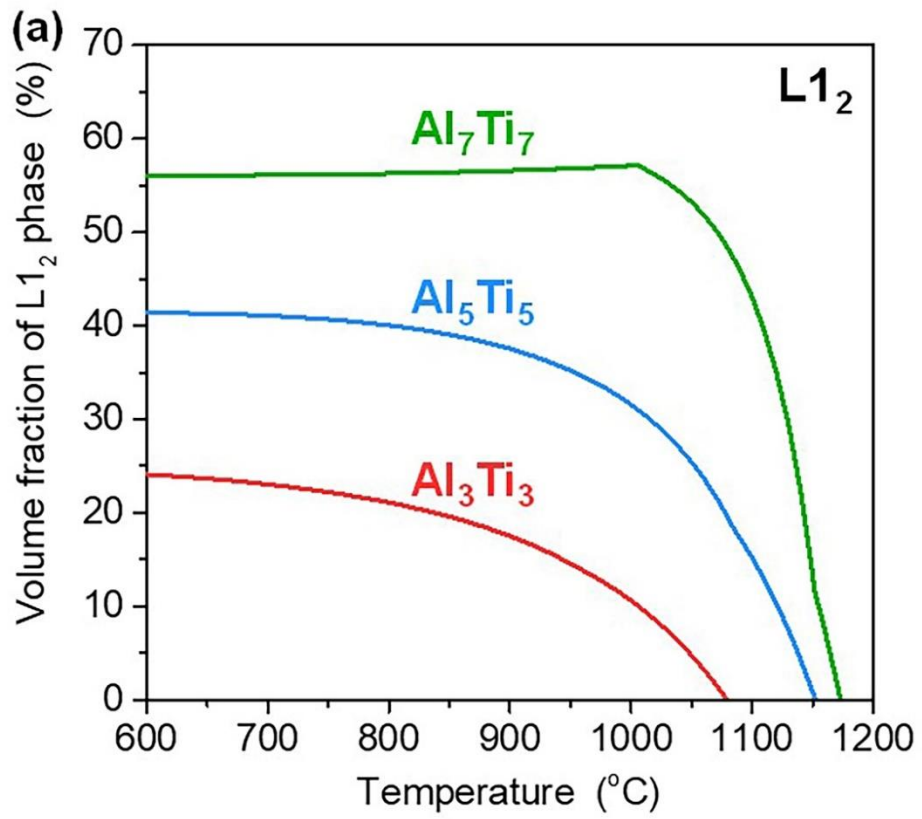


Fig. 12

